Journal of Innovative Optical Health Sciences
Vol. 7, No. 2 (2014) 1350057 (12 pages)

DOI: 10.1142/S1793545813500570

Adaptive *hp* finite element method for fluorescence molecular tomography with simplified spherical harmonics approximation

Hongbo Guo*, Yuqing Hou*, Xiaowei He*,‡, Jingjing Yu†,
Jingxing Cheng* and Xin Pu*
*School of Information Sciences and Technology
Northwest University, Xi'an, 710069, P. R. China
†School of Physics and Information Technology
Shaanxi Normal University, Xi'an, 710062, P. R. China
‡hexw@nwu.edu.cn

Received 12 July 2013
Accepted 15 September 2013
Published 12 November 2013

Recently, the simplified spherical harmonics equations (SP_N) model has attracted much attention in modeling the light propagation in small tissue geometries at visible and near-infrared wavelengths. In this paper, we report an efficient numerical method for fluorescence molecular tomography (FMT) that combines the advantage of SP_N model and adaptive *hp* finite element method (*hp*-FEM). For purposes of comparison, *hp*-FEM and *h*-FEM are, respectively applied to the reconstruction process with diffusion approximation and SP_N model. Simulation experiments on a 3D digital mouse atlas and physical experiments on a phantom are designed to evaluate the reconstruction methods in terms of the location and the reconstructed fluorescent yield. The experimental results demonstrate that *hp*-FEM with SP_N model, yield more accurate results than *h*-FEM with diffusion approximation model does. The phantom experiments show the potential and feasibility of the proposed approach in FMT applications.

Keywords: Fluorescence molecular tomography; simplified spherical harmonics equations; reconstruction; adaptive finite element method.

1. Introduction

As an increasingly important tool for *in vivo* preclinical research, fluorescence molecular tomography (FMT) aims at the quantitative reconstruction of the 3D spatial distribution of a photon source inside an animal volume from the photon density detected on the surface of the animal. In this imaging modality, the photon source is typically a fluorescent probe tagging the molecule of interest.[1,2] An external excitation light source is needed to

trigger the emission of light. By reconstructing the targeted fluorescent probes with an inverse method one can achieve 3D imaging of molecular processes noninvasively.[3,4]

The reconstruction process of FMT depends on a forward model that depicts photon propagation in biological tissues.[5] The propagation of light through biological tissue can be accurately described by the radiative transfer equation (RTE).[6] But analytical solutions to the RTE cannot be found for biological tissue with heterogeneous optical properties and curved tissue geometries.[7] Although introducing Kirchhoff approximation (KA) enables analytical methods suitable for arbitrary geometries, the reconstruction accuracy of KA method is lower owing to its inherent error.[8] Consequently, some approximations to the RTE, such as the discrete ordinates (S_N) and spherical harmonics (P_N) equations have been established to overcome the constraints for directly solving the RTE.[9] Among them, the diffusion approximation (DA) is the most widely used model due to its computational efficiency. However, it is also known that the accuracy of the DA model is limited in regions of low or zero scattering and some regions which are close to the light source.[5] In, Ref. 10 a transport model based on the simplified spherical harmonics equations (SP_N) was proposed. It is demonstrated that SP_N can accurately model light propagation in small tissue geometries at visible and near-infrared wavelengths, yielding transport-like solution with acceptable computational costs.[10,11] Therefore, such higher-order approximations are preferable for *in vivo* small animal imaging.

Mathematically, FMT is an ill-posed inverse problem due to high degrees of absorption and scattering of photons propagating through tissue.[12] Consequently, reconstruction algorithms for FMT have to address the ill-posedness of the reconstruction problem,[13] considering the fact that probes used in FMT are designed to accumulate in specific areas of interest, e.g., tumors or cancerous tissue. Consequently, the reconstructed images tend to be very sparse.[14] Recently, a variety of reconstruction algorithms with sparsity-promoting regularizers have been reported in the field of FMT, which yield improved reconstruction results.[5,15–17] These works also indicate that sparse reconstruction algorithms combined with more accurate forward model are appealing to accurate FMT reconstruction.

Stable numerical techniques for solving the forward model as well as fast inversion algorithms are crucial to reconstruction problem of FMT. As a typical numerical technique adaptive finite element methods (AFEM) has been intensively used in tomographic imaging. The adaptive mesh refinement techniques not only improve localization and quantification of sources but also enhance the robustness and efficiency of reconstruction.[4] The most widely used AFEM is $h-$FEM, i.e., splitting elements in space while keeping their polynomial degree fixed. *hp*-FEM is another version that uses a suitable combination of *h*-refinements (dividing elements into smaller ones) and *p*-refinements (increasing their polynomial degree). The exponential convergence makes *hp*-FEM a very attractive choice in field of solving partial differential equations.[18–20]

In this paper, we present an efficient reconstruction scheme for FMT based on the SP_N model. In the inverse process, the *hp*-FEM is coupled with a hybrid sparse reconstruction algorithm, which enables the reconstruction scheme to yield stable and fast reconstruction results.

The paper is organized as follows. In Sec. 2, we present the SP_N model and the *hp*-FEM-based sparse reconstruction algorithm. Section 3 elaborates on the experiments and results to validate the proposed reconstruction method. Finally, we give the discussions and conclusion in Sec. 4.

2. Method

2.1. *The simplified spherical harmonics approximation model*

The RTE for time domain problems is:

$$\frac{1}{c}\frac{\partial u}{\partial t}(r,t,\hat{s}) + \hat{s}\cdot\nabla u(r,t,\hat{s}) + \mu u(r,t,\hat{s}) = u_s\int_{4\pi} p(\hat{s},\hat{s}')u(r,t,\hat{s}')d\hat{s}' + q(r,t,\hat{s}), \quad (1)$$

where $u(r,t,\hat{s})$ is the radiance at point r, time t and in the direction of unit vector $\hat{s}\cdot\mu = \mu_s + \mu_a$, μ_s and μ_a are the absorption and scattering coefficients respectively, and c is the speed of light in the medium. The $p(\hat{s},\hat{s}')$ term is the scattering phase function and satisfies $\frac{1}{4\pi}\int_{4\pi} p(\hat{s}\cdot\hat{s}')d\hat{s}' = 1$. It characterizes the intensity of a beam which scatters from direction $\hat{s}'$ into direction $\hat{s}$. As a kind of widely used phase function, Henyey–Greenstein can

be expressed as[10]:

$$p(\cos\theta) = \frac{1-g^2}{4\pi(1+g^2-2g\cos\theta)^{3/2}}. \tag{2}$$

This model is widely used because (i) it is accurate, (ii) it depends on a single adjustable parameter g, which is space-dependent, and (iii) it has the following simple Legendre polynomial expansion:

$$p(\cos\theta) = \sum_{n=0}^{\infty} \frac{2n+1}{4\pi} g^n p_n(\cos\theta). \tag{3}$$

The SP_N approximation is hypothesized as the multidimensional generalization of the 1D P_N equations. After a series of deductions with the P_N method, the SP_N approximation is obtained,

$$\begin{aligned} &-\left(\frac{n+1}{2n+1}\right)\nabla\cdot\frac{1}{\mu_{a,n+1}}\nabla\left(\left(\frac{n+2}{2n+3}\right)\phi_{n+2}+\left(\frac{n+1}{2n+3}\right)\phi_n\right)\\ &-\left(\frac{1}{2n+1}\right)\nabla\cdot\frac{1}{\mu_{a,n-1}}\nabla\left(\left(\frac{n}{2n-1}\right)\phi_n+\left(\frac{n-1}{2n-1}\right)\phi_{n-2}\right)\\ &+\mu_{a,n}\cdot\phi_n = S, \end{aligned} \tag{4}$$

where $\mu_{a,n} = \mu_a + \mu_s(1-g^n)$. When ψ is expanded by the P_N approximation, ϕ_n are the Legendre moments of ψ.

Here, we present the formal derivation of the SP_3 equations for the case of fully anisotropic scattering.

$$\begin{aligned} &-\nabla\cdot\frac{1}{3\mu_{a1}}\nabla\phi_1+\mu_a\phi_1-\left(\frac{2}{3}\mu_a\right)\phi_2 = S\\ &-\nabla\cdot\frac{1}{7\mu_{a3}}\nabla\phi_2+\left(\frac{4}{9}\mu_a+\frac{5}{9}\mu_{a2}\right)\phi_2-\frac{2}{3}\mu_a\phi_1\\ &\quad = -\frac{2}{3}S. \end{aligned} \tag{5}$$

The Robin-type boundary conditions are implemented on the boundary:

$$\begin{aligned} &\left(\frac{1+B_1}{3\mu a_1}\right)n\cdot\nabla\phi_1-\left(\frac{D_1}{\mu a_3}\right)n\cdot\nabla\phi_2\\ &\quad = -\left(\frac{1}{2}+A_1\right)\phi_1+\left(\frac{1}{8}+C_1\right)\phi_2\\ &\frac{D_2}{\mu a_1}n\cdot\nabla\phi_1+\left(\frac{1+B_2}{7\mu a_3}\right)n\cdot\nabla\phi_2\\ &\quad = \left(\frac{1}{8}+C_2\right)\phi_1-\left(\frac{7}{24}+A_2\right)\phi_2. \end{aligned} \tag{6}$$

2.2. *The hp adaptive finite element algorithm*

For the h-version of the FEM, the polynomial degree k of the shape functions on the elements remains constant and the mesh size h decreases. This is in contrast to the p-version of the FEM in which the polynomial degree k increases and the mesh size h is constant. The hp-FEM can reduce the mesh size and increase the order interpolation basis functions on each mesh level synchronously, and thus a faster rate of convergence than the h-version can be obtained.[20–22]

In the framework of the adaptive hp-FEM, let $\{\Psi^1(x), \Psi^2(x), \ldots, \Psi^p(x), \ldots\}$ be interpolation basis functions with different orders at different mesh levels. When only considering the kth mesh level, the continuous field ϕ can be discretized with its values at a finite number of points in the region of interest

$$\phi \approx \phi^k = \sum_{i=1}^{N} \varphi_i^k(x)\Psi_i^p(x). \tag{7}$$

Similarly, the source $S(x)$ is discretized on the same finite element mesh as:

$$S(x) \approx S^k(x) = \sum_{i=1}^{N} s_i^k(x)\gamma_i^p(x). \tag{8}$$

Using the finite element method, we have the final weighted matrix as literature[11]

$$J_m^+ = AX. \tag{9}$$

This is a linear relationship between the measured photon flux density and the unknown fluorescent yield. The system matrix $A \in R^{m\times n}(m \ll n)$ is usually ill-conditioned.

In the inverse process, the hp-FEM is coupled with a sparse reconstruction algorithm. Here, the hp-FEM is used for creating a multilevel mesh and speed up the convergence. In the first mesh level, the reconstruction region is discretized into a uniformly coarse mesh. As shown in Fig. 1(a), the region of the fluorescent target is much smaller than the reconstruction region. To enforce conditions of sparsity on reconstructed FMT images, l_1-norm regularizer is adopted in this study. The recovery of the unknown fluorescent concentration is fulfilled by solving the following optimization problem with the incomplete variables truncated conjugate

gradient algorithm (IVTCG)[23]:

$$\min\{\|J_m^+ - AX\|_2^2 + \lambda\|X\|_1\}, \tag{10}$$

where $\|X\|_1 = \sum_i |x_i|$ and λ is a regularization parameter.

In the subsequent refined mesh levels, the reconstruction region is sharply reduced and the fluorescent target distribution lacks obvious sparseness compared with the reduced reconstruction region, as shown in Figs. 1(b) and 1(c). Therefore, it is reasonable to take another inversion algorithm on the subsequent mesh levels. The Landweber iterative regularization is then performed for reconstruction.[19,24] Therefore, the proposed reconstruction scheme is actually a hybrid multilevel reconstructions process, which is summarized in Algorithm 1.

Algorithm 1

Step 1: $i = 1$, for the initial coarse mesh level L_1, reconstruct X_i using the IVTCG algorithm in the entire reconstruction region Ω.
Step 2: $i = i + 1$. If $2 \le i \le L_{\max}$, determine the permissible domain Ω_i of the fluorescent target distribution from the results on the coarser mesh by choosing nodes with large values. Else end the algorithm.
Step 3: Implement *hp*-FEM on the permissible domain Ω_i to obtain a finer mesh L_i.
Step 4: Reconstruct X_i in the reconstruction region Ω_i on the refined mesh level L_i by Landweber iterative.
Step 5: Go to Step 2.

3. Experiments and Results

In this section, four groups of experiments were designed to validate the proposed reconstruction method for FMT. First, a single fluorescent target reconstruction was performed. For comparison purpose, *hp*-FEM and *h*-FEM are respectively applied in the reconstruction process with DA model and SP_N model. Secondly, we investigated the robustness and stability of our algorithm by considering the effects of optical parameters on the results. Thirdly, the performance of the developed method for double fluorescent targets was tested on a 3D digital mouse. The last is a physical phantom experiment for further evaluation of the proposed method.

All reconstructions were conducted on a personal computer with a 3 GHz Intel(R) Core(TM) 2 CPU E8400 and 2.00 GB RAM. To analyze the results quantitatively, location error (LE), the Euclidean distance between the centers of the reconstructed and the actual target is defined by $LE = [(x - x_0)^2 + (y - y_0)^2 + (z - z_0)^2]^{1/2}$, where (x, y, z) is the reconstructed source coordinate and (x_0, y_0, z_0) is the actual one.

3.1. *3D digital mouse simulations for a single fluorescent target*

The simulation experiments were conducted on a digital mouse atlas of CT and cryosection data, which provided anatomical information.[25] The torso of the mouse with a height of 35 mm was the

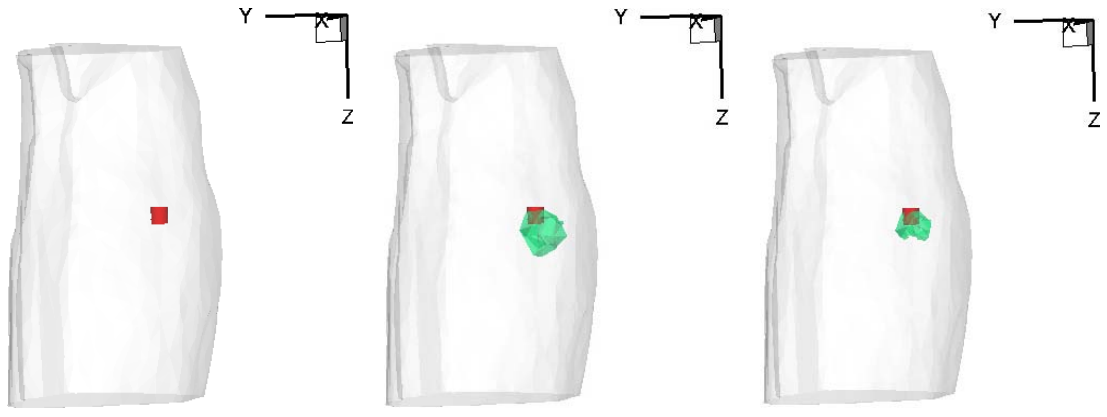

(a) (b) (c)

Fig. 1. Different reconstruction regions at different mesh levels. The red cylinder is the fluorescent target. (a) The reconstruction region for the first mesh level consists of the entire mouse torso. (b) The green zone is the reconstruction region at the second level. (c) The green zone is the reconstruction region at the third level.

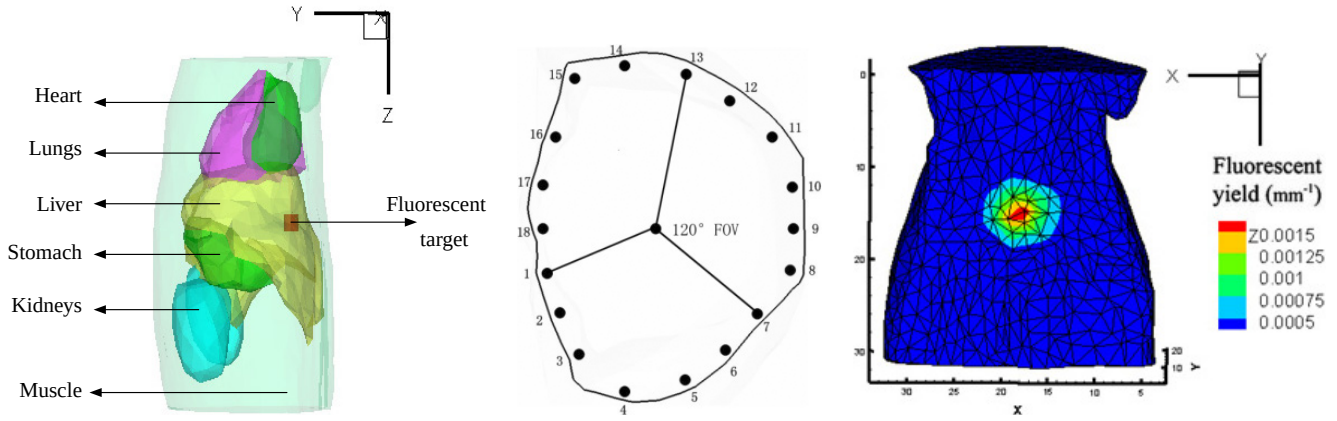

Fig. 2. (a) Torso of the mouse atlas model with a cylindrical fluorescent target in the liver. (b) The plane of excitation sources at $z = 16.4$ mm and the black points represent the location of the isotropic point sources. (c) Mesh for generating synthetic measurements and photon distribution on surface.

region to be investigated, shown in Fig. 2. A cylindrical fluorescent target with a 0.8-mm radius and 1.6-mm height was placed in the liver with center at (11.9, 6.4, 16.4 mm), as shown in Fig. 1(a), and the fluorescent yield of the fluorescent target was set to be 0.05 mm^{-1}. To generate the synthetic measurements on the boundary, the model was discretized into tetrahedral-element mesh consisting of 132,202 elements and 24,906 nodes. The optical parameters for different organs are presented in Table 1.[26] Obviously, in this case, scattering effects within the region of interest are dominant over absorption effects, i.e., $\mu_s' \gg \mu_a$. In this experiment, the fluorescent target was excited by 18 point-sources at different positions in sequence, as shown in Fig. 2(b). The black dots represent positions of the excitation point sources, which were modeled as isotropic point sources located one mean free path of photon transport beneath the surface on the $z = 16.4$-mm plane. For each excitation source, the surface data on the opposite side with a 120° field of view (FOV) were measurable. Measurements were obtained every 20° and a total of 18 datasets were assembled for the reconstruction of the fluorescent yield.

Table 1. Optical parameters of the mouse organs (highly scatter).

Tissue	$\mu_{ax}(\text{mm}^{-1})$	$\mu_{sx}^{'}(\text{mm}^{-1})$	$\mu_{am}(\text{mm}^{-1})$	$\mu_{sm}^{'}(\text{mm}^{-1})$
Muscle	0.0052	1.08	0.0068	1.03
Heart	0.0083	1.01	0.0104	0.99
Lungs	0.0133	1.97	0.0203	1.95
Liver	0.0329	0.70	0.0176	0.65
Kidneys	0.0660	2.25	0.0380	2.02
Stomach	0.0114	1.74	0.0070	1.36

For the inverse problem, the maximum mesh level $L_{\max}$ was set to 3. The digital mouse model was discretized into 9518 tetrahedral elements and 2032 nodes as the coarse mesh. We employed the IVTCG algorithm for the reconstruction on the first mesh and selected the regularization parameter $1e-10$. The stopping criterion for the IVTCG algorithm is $\|J_m^+ - AX\|_2^2 \leq 1e-12$. For the following reconstruction on the refined mesh, the Landweber iteration is then performed. It will stop the iteration when the relative residual is less than a given threshold, or it reaches the maximum number of iterations. We set the threshold value $5e-3$, and the maximum number of iterations to 500 in the following experiments.

In all experiments, we selected the largest value of $X(r)$ as the reconstructed fluorescent yield, and recognized the node with the largest reconstructed value as the center of the fluorescent target. The nodes with the reconstructed value bigger than 80% of the largest value were picked out to form the permissible region for next reconstruction.

To reveal the impact of the forward model on FMT reconstruction, we compared the reconstructed results with different forward models on the first coarse mesh level, as shown in Fig. 3. The quantitative comparison is in Table 2. These results

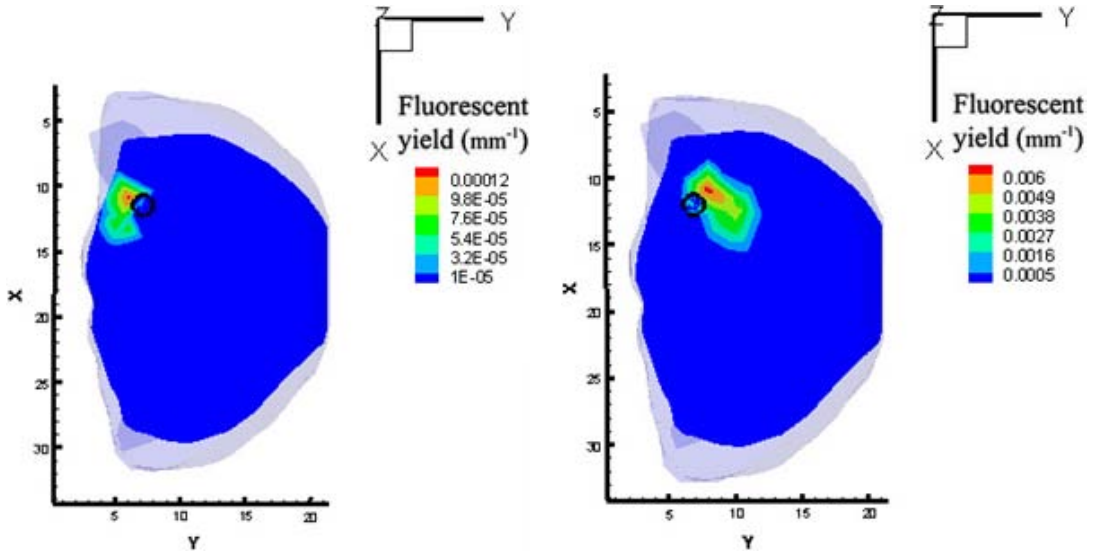

(a) (b)

Fig. 3. Reconstructed results with different forward models on the first mesh level. (a) SP_N model. (b) DA model.

Table 2. Reconstructed results in single target case on the initial coarse mesh (highly scattering media).

Forward model	Actual position center (mm)	Reconstruction position center (mm)	LE (mm)	Reconstruction fluorescent yield (mm^{-1})
DA	(11.9,6.4,16.4)	(10.7,7.3,16.4)	1.56	0.006
SP_N	(11.9,6.4,16.4)	(11.3,5.3,16.4)	1.26	0.0013

illustrate a better performance of the SP_N model in location accuracy, whereas the reconstructed fluorescent yield is inferior to that of DA model. In general, the reconstruction results on the initial coarse mesh are unsatisfactory, and therefore it is necessary to conduct multilevel reconstruction based on adaptive FEM. The final reconstruction by the proposed method for the single target is presented in Fig. 4(a).

In addition, to investigate the influence of *hp*-FEM on the reconstruction, we compared it with *h*-FEM. The ultimate refined mesh in the *hp*-FEM and *h*-FEM has 10,206 tetrahedral elements and 3145 nodes. The comparison results on the final mesh are shown in Fig. 4 and Table 3. The results show that: (1) Generally, two forward models combined with two FEMs can estimate the position of fluorescence sources; (2) The proposed method, *hp*-FEM with SP_N model, yield more accurate results than *h*-FEM with DA model does. (3) Compared with *h*-FEM, *hp*-FEM converges faster when the mesh is refined.

3.2. *3D digital mouse simulations for a single fluorescent target with strong absorption*

As mentioned above, DA model is limited in some low or zero scattering regions and SP_N model can improve the diffusion solution in transport-like domains with strong absorption and small geometries. So we also validate the advantages of the SP_N model by taking into consideration the influence of optical parameters. A set of typical optical properties were considered here, as listed in Table 4.[27] Different from the parameters in Table 1, scattering effects within interesting region are not dominant over absorption effects.

The reconstruction results are shown in Fig. 5. The location error and reconstructed fluorescent yield are presented in Table 5. It is obvious that in regions of strong absorption, the result by DA model significantly deviates from the actual position center and the model error is approximately up to two times larger than that of the SP_N model.

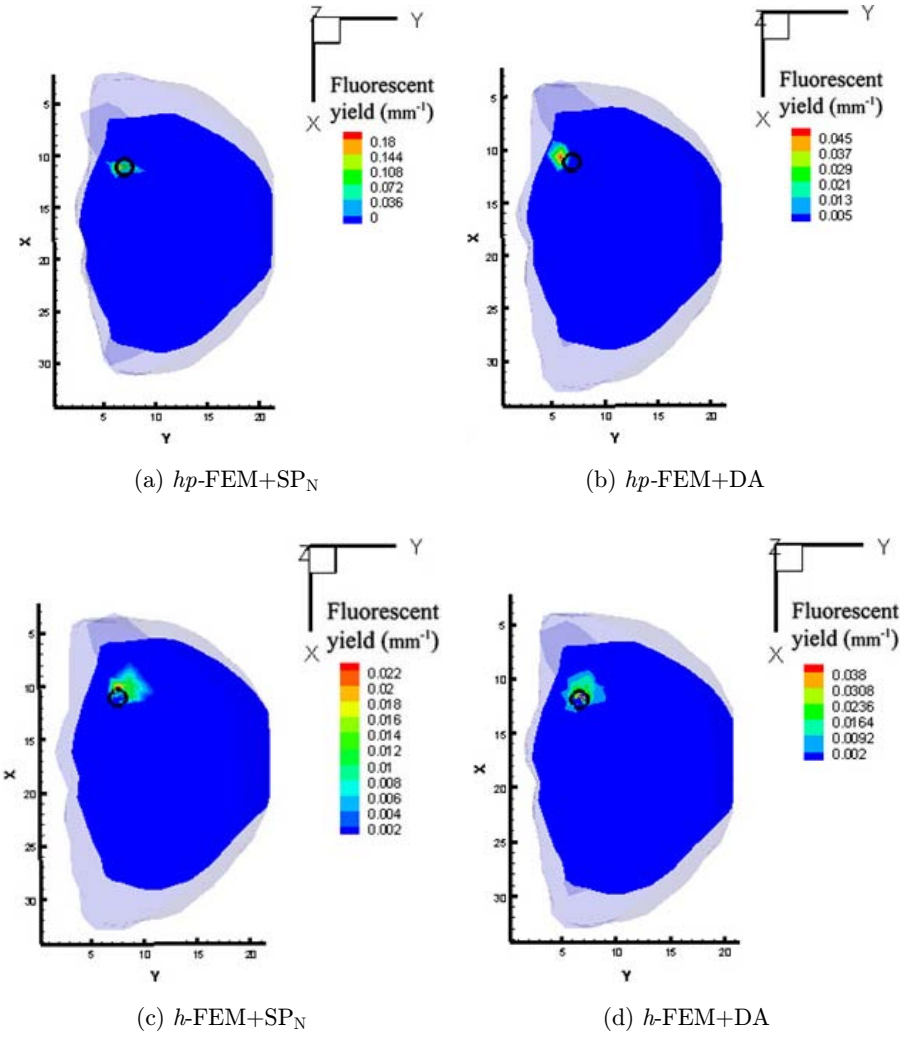

(a) *hp*-FEM+SP_N (b) *hp*-FEM+DA

(c) *h*-FEM+SP_N (d) *h*-FEM+DA

Fig. 4. A comparison of *hp*-FEM and *h*-FEM on different forward model. (a) and (c) are the transverse views of the reconstruction result using *hp*-FEM and *h*-FEM on the SP_N model. (b) and (d), are the corresponding results of them on the DA model.

3.3. *Reconstruction of double fluorescent targets*

We also conducted double fluorescent targets experiments with the mouse model. Two fluorescent targets were located in the liver with centers at (11.9, 6.4, 16.4 mm) and (11.9, 10.9, 16.4 mm). The initial mesh, the optical parameters and the fluorescent yield were the same as the single target case in Experiment A. The final refined mesh for double fluorescent targets consists of 10,093 tetrahedral elements and 2132 nodes. The reconstructed results are presented in Fig. 6 and Table 6. It can be inferred from Fig. 6 that the *hp*-FEM makes two targets that could be resolved clearly. On the initial

Table 3. Quantitative comparison between *hp*-FEM and *h*-FEM.

Forward model	FEM	Actual position center (mm)	Reconstruction position center (mm)	LE (mm)	Actual fluorescent yield (mm^{-1})	Reconstruction fluorescent yield (mm^{-1})
DA	*h*-FEM	(11.9,6.4,16.4)	(11.4,5.7,16.0)	0.94	0.05	0.025
	***hp*-FEM**	**(11.9,6.4,16.4)**	**(11.6,6.7,15.9)**	**0.62**	**0.05**	**0.039**
SP_N	*h*-FEM	(11.9,6.4,16.4)	(11.0,6.4,16.4)	0.91	0.05	0.022
	***hp*-FEM**	**(11.9,6.4,16.4)**	**(11.8,6.2,16.0)**	**0.51**	**0.05**	**0.049**

Table 4. Optical parameters of the mouse organs (highly absorbing media).

Tissue	$\mu_{ax}(\mathrm{mm}^{-1})$	$\mu'_{sx}(\mathrm{mm}^{-1})$	$\mu_{am}(\mathrm{mm}^{-1})$	$\mu'_{sm}(\mathrm{mm}^{-1})$
Muscle	0.22	1	0.22	1
Heart	0.11	1.01	0.11	1.01
Lungs	0.35	2.30	0.35	2.30
Liver	0.45	2	0.45	2
Kidneys	0.12	1.2	0.12	1.2
Stomach	0.21	1.7	0.21	1.7

coarse mesh, both of the reconstructions fail in discriminating the two targets, as shown in Figs. 6(b) and 6(f). However, on the subsequent meshes, the *hp*-FEM with SP_N model and DA model finally resolve the two targets successfully, as shown in Figs. 6(d) and 6(h). Moreover, *hp*-FEM combined with SP_N model has a better performance in the location and the reconstructed fluorescent yield.

3.4. *Physical experiments*

Physical experiments were also conducted to further evaluate the proposed reconstruction method. A cubic phantom with a side length of 20 mm is used, as shown in Fig. 7. The phantom was made from polyoxymethylene. To obtain a testing fluorescent target, a small hole with 1-mm radius and 2-mm height was drilled to emplace the 4000-nM Cy5.5 solution (with the extinction coefficient of about $0.019\,\mathrm{mm}^{-1}\mu\mathrm{M}^{-1}$ and the quantum efficiency of 0.23 at the peak excitation wavelength of 671 nm[28]).

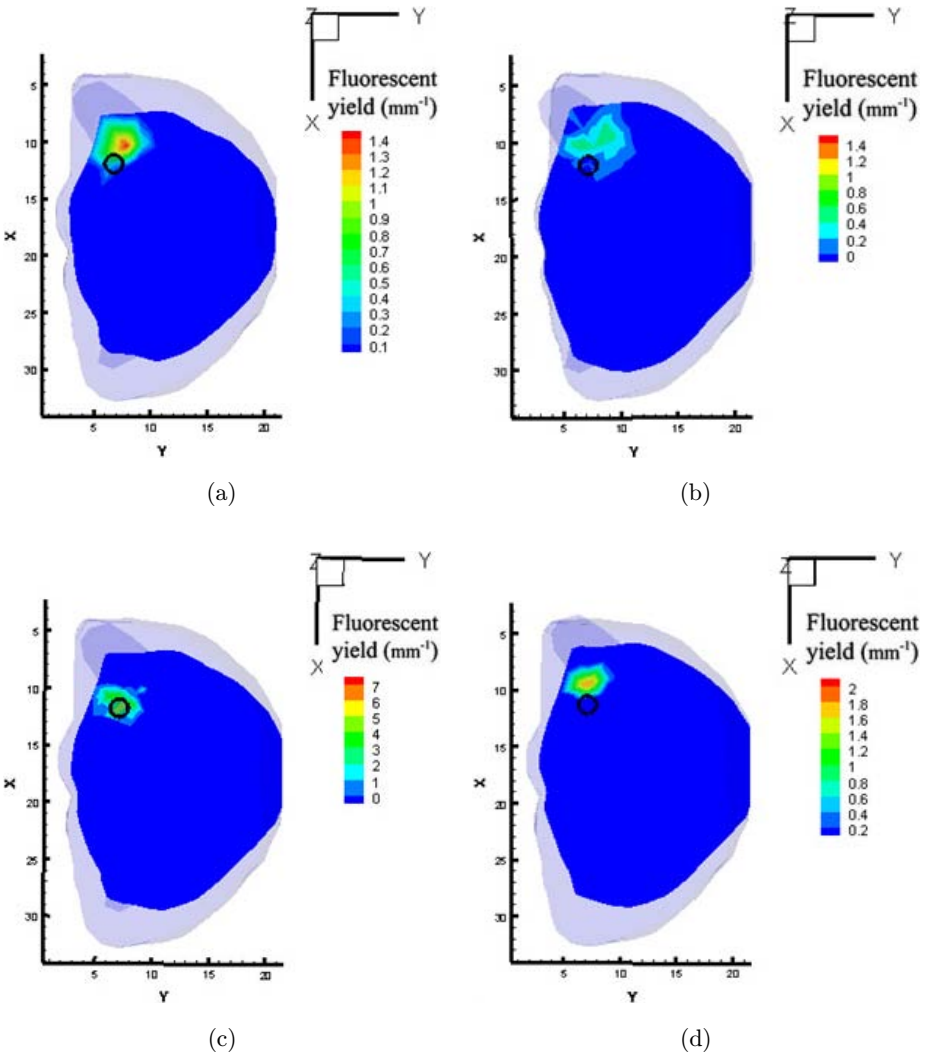

Fig. 5. Transverse view of the reconstruction results in highly absorbing media, where the black circles represent the real target. (a) Result of SP_N model on the initial mesh level. (b) Result of DA model on the initial mesh level. (c) Final result of SP_N model with *hp*-FEM. (d) Final result of DA model with *hp*-FEM.

Table 5. Results in single target case on the final mesh (highly absorbing media).

Forward model	Actual position center (mm)	Reconstruction position center (mm)	LE (mm)
DA	(11.9,6.4,16.4)	(10.7,5.7,15.4)	1.79
SP_N	(11.9,6.4,16.4)	(11.3,5.8,15.8)	1.06

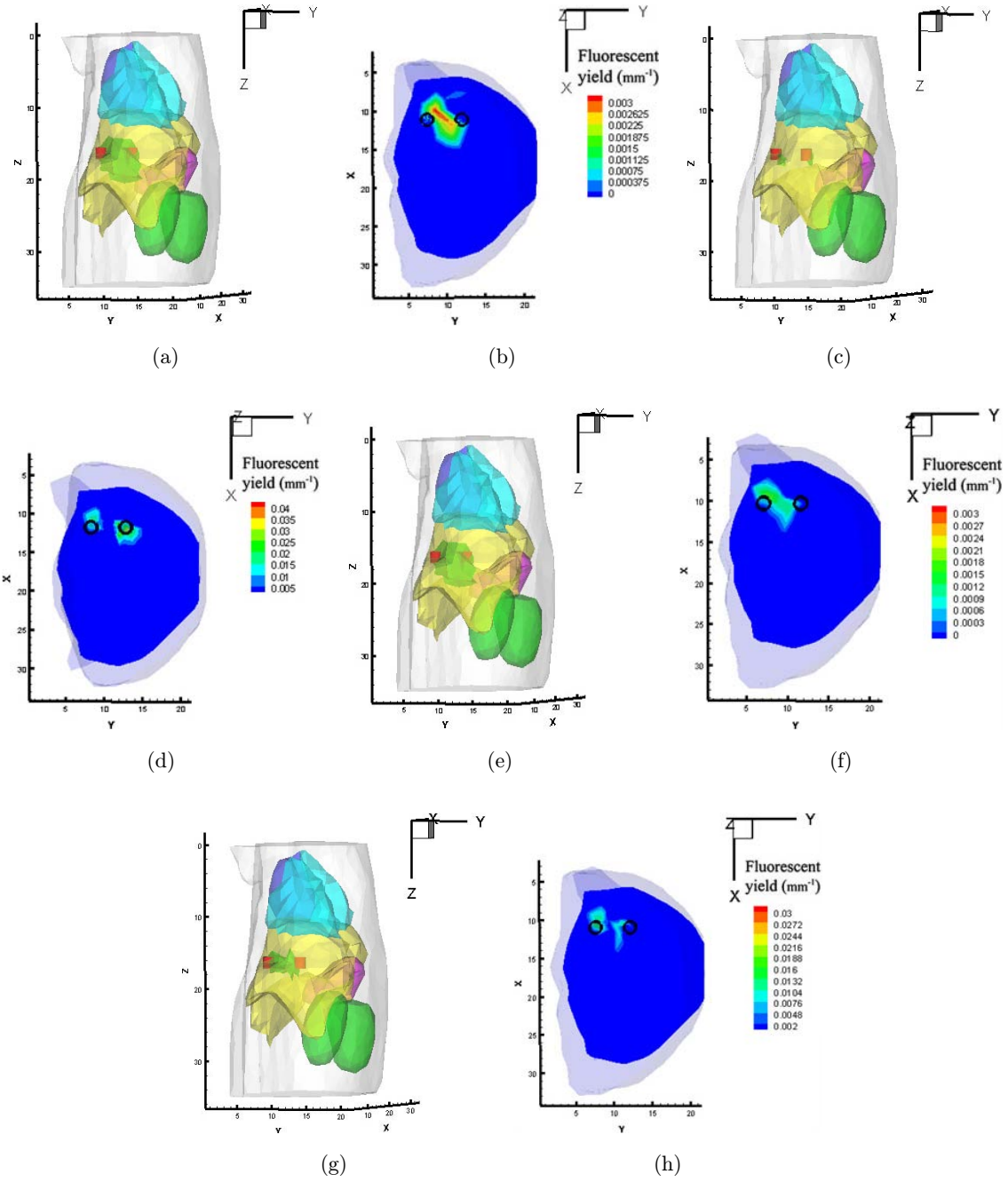

Fig. 6. Reconstruction results for double fluorescent targets embedded in the liver. (a) and (b) are the isosurface view and transverse view of the results on the initial coarse mesh with SP_N model. (c) and (d) are the results of the SP_N model with *hp*-FEM on the final mesh. (e) and (f) are the results on the initial coarse mesh with DA model. (g) and (h) are the results the DA model with *hp*-FEM on the final mesh.

Table 6. Quantitative results of our method for double targets on final mesh.

Forward model	Target	Actual position center (mm)	Reconstruction position center (mm)	LE (mm)	Actual fluorescent yield (mm^{-1})	Reconstruction fluorescent yield (mm^{-1})
SP_N	Target 1	(11.9,10.9,16.4)	(12.5,10.7,16.8)	0.79	0.05	0.045
	Target 2	(11.9,6.4,16.4)	(11.7,6.4,16.7)	0.36	0.05	0.026
DA	Target 1	(11.9,10.9,16.4)	(12.0,10.0,16.5)	1.03	0.05	0.026
	Target 2	(11.9,6.4,16.4)	(11.7,6.9,17.03)	0.9	0.05	0.026

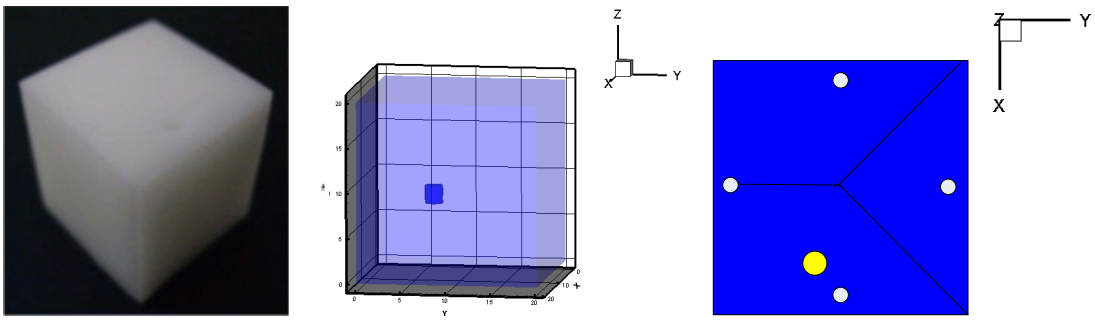

(a) (b) (c)

Fig. 7. Physical phantom. (a) The 3D view of the single fluorescent target in the cubic phantom. (b) The 3D view of the single fluorescent target in the cubic phantom. (c) The x–y view on the $z = 10$-mm plane, where the white dots represent the excitation point source positions.

The coordinate of the hole center was (16, 8, 9.5 mm), as shown in Fig. 7(b).

The fluorescent target was excited by point sources from four different positions at the $z =$ 10-mm plane, as shown in Fig. 7(c). And a CCD camera (Princeton Instruments PIXIS 2048B, Roper scientific, Trenton, New Jersey) was used to capture the signal on the phantom surface from four views by rotating the phantom with an angular increment of 90°. The optical properties for both excitation and emission wavelengths are listed in Table 7.[19]

Table 7. Optical properties of the homogeneous cubic phantom.

Wavelength (nm)	$\mu_a(mm^{-1})$	$\mu_s'(mm^{-1})$
671	0.00029	1.08
710	0.00051	1.11

During the reconstruction process, the cubic phantom was discretized into 14,780 tetrahedral elements and 2989 nodes as the initial coarse mesh. With the proposed hybrid multilevel reconstruction

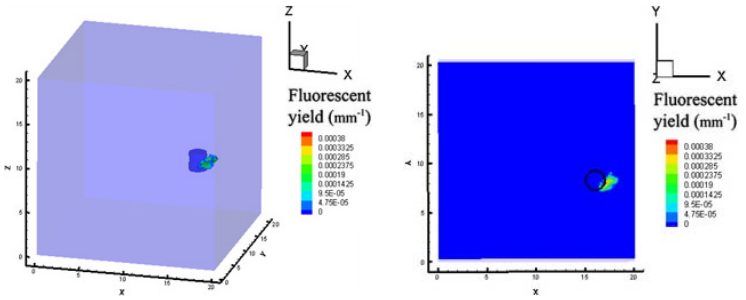

(a) (b)

Fig. 8. Phantom results. (a) The isosurface view of the reconstruction with top 80% of the maximum value. The blue cylinder represents the real Cy5.5 solution, while the green zone is the reconstructed target. (b) The transverse view of the reconstruction is on the $z = 9.5$-mm plane. The black circle represents the real target.

method, we yield successful reconstruction. Reconstruction results are shown in Fig. 8, with the reconstructed coordinate (16.8, 7.6, 9.5 mm) and location error 0.89 mm. The reconstructed concentration of Cy5.5 dye is about 616.9 nM. Figure 8(b) is the transverse view of the reconstruction result at the $z = 9.5$ mm-plane.

4. Discussion and Conclusion

In this paper, we adopt a higher-order approximation of RTE to model the light propagation in tissue for tomographic fluorescent imaging. Compared with DA, SP_N model tends to produce more accurate reconstruction results, especially in highly absorbing media which is illustrated by our numerical study in Sec. 3.

The reconstruction results in this work, especially for double targets case, demonstrate the merits and potential of the *hp*-FEM for FMT. Owing to the use of *hp*-FEM, the proposed reconstruction method not only accurately reconstructs the single fluorescent target but also successfully distinguishes the double fluorescent targets.

The contribution of this work is that an efficient numerical method for FMT that combines the advantage of SP_N forward model and *hp*-FEM is proposed. Numerical simulations illustrate that the proposed method enable accurate and stable recovery of fluorescent targets. In future, acceleration strategies and *in vivo* experiments of this hybrid multilevel reconstruction method will be further investigated.

Acknowledgments

This work is supported by the National Natural Science Foundation of China (Grant No. 61372046), the Research Fund for the Doctoral Program of Higher Education of China (New Teachers) (Grant No. 20116101120018), the China Postdoctoral Science Foundation Funded Project (Grant Nos. 2011M501467 and 2012T50814), the Natural Science Basic Research Plan in Shaanxi Province of China (Grant No. 2011JQ1006), the Fundamental Research Funds for the Central Universities (Grant No. GK201302007), Science and Technology Plan Program in Shaanxi Province of China (Grant Nos. 2012 KJXX-29 and 2013K12-20-12), the Science and Technology Plan Program in Xi'an of China (Grant No. CXY1348(2)), the Graduate Innovation Project of Northwest University (Grant No. YZZ12093), and the Science and Technology Program of Educational Committee of Shaanxi Province of China (Grant No. 12JK0729).

References

1. V. Ntziachristos, J. Ripoll, L. V. Wang, R. Weisslder, "Looking and listening to light: The evolution of whole body photonic imaging," *Nat. Biotechnol.* **23**, 313–320 (2005).
2. J. Tian, J. Bai, X. Yan, S. Bao, Y. Li, W. Liang, X. Yang, "Multimodality molecular imaging," *IEEE Eng. Med. Biol. Mag.* **27**, 48–57 (2008).
3. Y. Lin, W. C. Barber, J. S. Iwanczyk, W. W. Roeck, O. Nalcioglu, G. Gulsen, "Quantitative fluorescence tomography using a trimodality system: In vivo validation," *J. Biomed. Opt.* **15**, 040503 (2010).
4. X. Song, D. Wang, N. Chen, J. Bai, H. Wang, "Reconstruction for free-space fluorescence tomography using a novel hybrid adaptive finite element algorithm," *Opt. Express* **15**, 18300–18317 (2007).
5. D. Han, J. Tian, K. Liu, J. Feng, B. Zhang, X. Ma, C. Qin, "Sparsity promoting tomographic fluorescence imaging with simplified spherical harmonics approximation," *IEEE Trans. Biomed. Eng.* **57**, 2564–2567 (2010).
6. Y. Lv, B. Zhu, H. Shen, J. C. Rasmussen, G. Wang, E. M. Sevick-Muraca, "A parallel adaptive finite element simplified spherical harmonics approximation solver for frequency domain fluorescence molecular imaging," *Phys. Med. Biol.* **55**, 4625–4645 (2010).
7. L. V. Wang, H. Wu, *Biomedical Optics: Principles and Imaging*, Wiley-Interscience, USA (2007).
8. X. Wang, X. Cao, B. Zhang, F. Liu, J. W. Luo, J. Bai, "A hybrid reconstruction algorithm for fluorescence tomography using Kirchhoff approximation and finite element method," *Med. Biol. Eng. Comput.* **51**, 7–17 (2013).
9. A. D. Klose, "The forward and inverse problem in tissue optics based on the radiative transfer equation: A brief review," *J. Quant. Spectrosc. Radiat. Transf.* **111**, 1852–1853 (2010).
10. A. D. Klose, E. W. Larsen, "Light transport in biological tissue based on the simplified spherical harmonics equations," *J. Comput. Phys.* **220**, 441–470 (2006).
11. A. D. Klose, E. W. Larsen, "Excitation-resolved fluorescence tomography with simplified spherical harmonics equations," *Phys. Med. Biol.* **56**, 443–1469 (2011).

12. A. X. Cong, "Reconstruction methods for optical molecular tomography," Dissertation, Virginia Polytechnic Institute and State University (2012).
13. A. Cong, G. Wang, "A finite-element-based reconstruction method for 3D fluorescence tomography," *Opt. Express* **13**, 847–9857 (2005).
14. S. Kossodo, M. Pickarski, S. A. Lin, A. Gleason, "Dual in vivo quantification of integrin-targeted and protease-activated agents in cancer using fluorescence molecular tomography," *Mol. Imaging Biol.* **12**, 488–499, (2010).
15. J. C. Baritaux, K. Hassler, M. Unser, "An efficient numerical method for general lp regularization in fluorescence molecular tomography," *IEEE Trans. Med. Imaging* **29**, 1075–1085 (2010).
16. J. W. Shi, X. Cao, F. Liu, B. Zhang, J. W. Luo, J. Bai, "Greedy reconstruction algorithm for fluorescence molecular tomography by means of truncated singular value decomposition conversion," *J. Opt. Soc. Am. A* **30**, 437–447 (2013).
17. D. Han, J. Tian, S. Zhu, J. Feng, Ch. Qin, B. Zhang, X. Yang. "A fast reconstruction algorithm for fluorescence molecular tomography with sparsity regularization," *Opt. Express* **18**, 8630–8646 (2010).
18. R. Han, J. Liang, X. Qu, Y. Hou, N. Ren, J. Mao, J. Tian, "A source reconstruction algorithm based on adaptive *hp*-FEM for bioluminescence tomography," *Opt. Express* **17**, 14481–14494 (2009).
19. H. Yi, D. Chen, X. Qu, K. Peng, X. Chen, Y. Zhou, J. Tian, J. Liang, "Multilevel, hybrid regularization method for reconstruction of fluorescent molecular tomography," *Appl. Opt.* **51**, 975–986 (2012).
20. I. Babuska, B. Q. Guo, "The h, p and h-p version of the finite element method: Basis theory and applications," *Adv. Eng. Softw.* **15**, 159–174 (1992).
21. J. M. Melenk, *hp-Finite Element Methods for Singular Perturbations*, Springer-Verlag, Berlin (2002).
22. C. Schwab, *p- and hp-Finite Element Methods: Theory and Applications in Solid and Fluid Mechanics*, Numerical Mathematics and Scientific Computation, Clarendon Press, Oxford (1998).
23. X. He, J. Liang, X. Wang, J. Yu, X. Qu, X. Wang, Y. Hou, D. Chen, F. Liu, J. Tian, "Sparse reconstruction for quantitative bioluminescence tomography based on the incomplete variables truncated conjugate gradient method," *Opt. Express* **18**, 24825–24841 (2010).
24. W. Q. Yang, D. M. Spink, T. A. York, H. McCann, "An image-reconstruction algorithm based on Landweber's iteration method for electrical-capacitance tomography," *Meas. Sci. Technol.* **10**, 1065–1069 (1999).
25. B. Dogdas, D. Stout, A. F. Chatziioannou, R. M. Leahy, "Digimouse: A 3D whole body mouse atlas from CT and cryosection data," *Phys. Med. Biol.* **52**, 577–587 (2007)
26. G. Alexandrakis, F. R. Rannou, A. F. Chatziioannou, "Tomographic bioluminescence imaging by use of a combined optical-PET (OPET) system: A computer simulation feasibility study, " *Phys. Med. Biol.* **50**, 4225–4241 (2005).
27. D. Wang, X. Liu, Y. Chen, J. Bai, "A novel finite element based algorithm for fluorescence molecular tomography of heterogeneous media," *IEEE Trans. Inf. Technol. Biomed.* **13**, 766–773 (2009).
28. Y. Lin, H. Gao, O. Nalcioglu, G. Gulsen, "Fluorescence diffuse optical tomography with functional and anatomical a priori information: Feasibility study," *Phys. Med. Biol.* **52**, 5569–5585 (2007).